Passivation of Grid-Following VSCs: A Comparison Between Active Damping and Multi-Sampled PWM

Ivan Z. Petric, *Student Member, IEEE*, Paolo Mattavelli, *Fellow, IEEE*, and Simone Buso, *Member, IEEE*

***Abstract*—This article compares different strategies used to enhance the stability properties of grid-following voltage-source converters (VSCs). Because of digital delays, VSC admittance exhibits a nonpassive zone, which introduces negative damping and may destabilize the grid-connected operation. It is shown that typically used active damping (AD) strategies only bring positive impact up to a certain frequency, while deteriorating admittance properties around and above the Nyquist frequency. Multi-sampled pulsewidth modulation (MS-PWM) greatly extends the passive admittance region, using only a single-loop current controller. Experimental admittance measurements are performed on a single-phase VSC, up to twice the switching frequency. Subsequently, different grid-connected scenarios are tested to show that MS-PWM retains stable operation, where AD methods cause instability. This article also offers analytic modeling and experimental measurements of noise propagation for compared strategies. It is shown that derivative-based AD is not highly sensitive; however, MS-PWM offers additional noise suppression.**

***Index Terms*—Active damping (AD), multi-sampled pulsewidth modulation (MS-PWM) control, passivity, voltage-source converters (VSCs).**

I. Introduction

GRID-FOLLOWING voltage-source converters (VSCs) are becoming increasingly present in electric energy distribution grids [1], [2]. However, connecting an actively controlled VSC to a grid may bring stability issues [3]. One of such problems may arise when poorly damped grid resonances get destabilized due to current-loop dynamics of the connecting VSC [3]. This article focuses on the investigation of harmonic instability at high frequencies, which is enabled by delays of the current control system [4], [5]. To prevent the harmonic instability, passivity-based control (PBC) has gained significant attention [5]–[27]. Starting from impedance-based stability assessment [28]–[31], PBC provides a sufficient condition for stability by rendering the VSC input admittance passive, i.e., making its real part nonnegative. This concept has proved to be powerful for the analysis and improvement of the stability of a system that consists of many interconnected power converters [3], [7], [32]–[34]. Initially, the authors focused on passivizing the admittance up to the Nyquist frequency (NF). However, more recently, it has been pointed out that passivity should be investigated also above the NF, where coupling between sidebands, generated by sampling and modulation, introduces a destabilizing mechanism [18], [27], [35], [36].

The focus of this article is placed on the most widely used VSCs that operate using pulsewidth modulation (PWM). For uniformly sampled PWM (US-PWM) [4] with one step computation delay, VSC admittance exhibits negative conductance above one-sixth of the sampling frequency f_s [16]. For enhancing the passivity, many different strategies of active damping (AD) have been developed. Some improvement is obtained by adding damping filters to the current controller (CC) [6]–[9]; however, most methods employ additional feedforward or feedback actions [10]–[26]. Although certain multiloop methods are developed specifically for VSCs with LCL filters [10]–[15], this article compares and refers to the most generally applicable ones that are relevant also for VSCs with L filters [16]–[19]. These methods rely on the derivative-based feedforward of the voltage at the point of common coupling (PCC). In terms of effectiveness, for full passivity up to the NF, analog or oversampled derivative action must be applied. This kind of AD, first analyzed in [16] and generalized in [19], will be referred to as the derivative active damping (D-AD). The passive region can also be extended without analog or oversampled implementation, which is referred to as discretized derivative active damping (DD-AD) [17], [18]. DD-AD effectively increases the passive region up to approximately $f_s/3$. Another important fact is that, for any AD implementation, passivity enhancement is affected by parameter mismatch. An alternative approach to US-PWM is the multi-sampled PWM (MS-PWM), where the control action is executed at a rate higher than double the switching frequency [37]–[54]. MS-PWM reduces control update and modulation delays and, in this way, approaches the naturally sampled PWM [55]. In [54], it is shown that MS-PWM inherently renders the admittance passive in a wide frequency range.

This article first compares the effectiveness of D-AD, DD-AD, and MS-PWM in passivizing the admittance near and above the switching frequency. Even though in [27], it is shown that this frequency range is important for stability, there is a lack of

Manuscript received 21 February 2022; revised 4 May 2022; accepted 1 June 2022. Date of publication 13 June 2022; date of current version 26 July 2022. This work was supported in part by the Italian Ministry for Education, University, and Research under project "Holistic approach to energy-efficient smart nanogrids" HEROGRIDS, under Grant PRIN 2017WA5ZT3 and in part by the MIUR (Italian Minister for Education) under the initiative "Departments of Excellence" (Law 232/2016). Recommended for publication by Associate Editor Y. Xue. *(Corresponding author: Ivan Z. Petric.)*

Ivan Z. Petric and Simone Buso are with the Department of Information Engineering, University of Padova, 35131 Padova, Italy (e-mail: ivan.petric@phd.unipd.it; simone.buso@dei.unipd.it).

Paolo Mattavelli is with the Department of Management and Engineering, University of Padova, 36100 Vicenza, Italy (e-mail: paolo.mattavelli@unipd.it).

Color versions of one or more figures in this article are available at https://doi.org/10.1109/TPEL.2022.3181935.

Digital Object Identifier 10.1109/TPEL.2022.3181935

detailed investigation of corresponding AD effectiveness, which is addressed in this article. Furthermore, a potential practical challenge with D-AD and DD-AD concerns noise sensitivity due to the implementation of the derivative feedforward action. Accordingly, this article provides an investigation of noise propagation, which has not been analyzed in the literature yet.

Main novelties and contributions of this article are summarized as follows.

1) *A comparative analysis of passivizing properties of D-AD, DD-AD, and MS-PWM:* It is experimentally validated that AD *does not* provide the robust stability of grid-tied VSCs for harmonic resonances around and above the NF. This property is predictable by a linear single-frequency model of the VSC admittance. Experimental results are given to show the destabilization of grid antiresonances found slightly below the NF for DD-AD and above NF for D-AD. MS-PWM enables stable operation for all tested cases by passivizing the VSC in a wider frequency range.
2) *Analytic modeling, experimental measurements, and comparison of noise sensitivity of D-AD, DD-AD, and MS-PWM:* The proposed analytics predict well the experimental measurements in case of both single- and double-loop control systems. Another step forward is taken by modeling the noise propagation for the case of oversampled (or analog) derivative being followed by a resampler, i.e., the case of D-AD. An important conclusion is that D-AD and DD-AD strategies *are not* highly sensitive to measurement noise, thanks to a relatively low required value of the derivative gain. For DD-AD, it is shown that, for all practical purposes, noise sensitivity is the same as without AD. Comparatively, MS-PWM is found to offer stronger noise suppression.

The rest of this article is organized as follows. Section II describes the current control system of a grid-following VSC and explains the impact of admittance on stability. Section III analyzes strategies for passivity enhancement and shows corresponding experimental admittance measurements. Section IV analyzes the implications of connecting a VSC with a nonpassive admittance to a grid. Experimental tests are provided to show that AD strategies cause instability for certain grid impedances. Section V analyzes noise propagation and shows corresponding measurements. Finally, Section VI concludes this article.

II. Control of Grid-Following VSCs

Grid-following VSCs are employed in power systems as current-controlled converters. As the most general case, this article considers a single-phase VSC with an inductive output filter, as shown in Fig. 1(a). However, the analysis is directly applicable to three-phase VSCs in stationary coordinates as well as to any output filter. The current reference $i_{L,r}$ is provided by outer loops that control the required power flow by changing the reference current magnitude $|i_{L,r}|$ and phase angle Φ, with respect to the voltage at the PCC, v_{pcc}. A phase-locked loop (PLL) is used to track the fundamental component of v_{pcc}. The CC processes the error between $i_{L,r}$ and the measured inductor current $i_{L,f}$. It may also include an action based on v_{pcc}, which

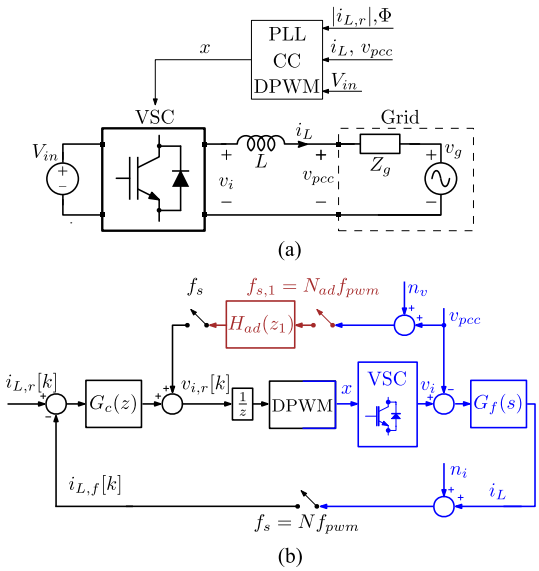

Fig. 1. Illustration of a grid-following VSC. (a) Schematic representing connection to a grid. (b) Multirate current control system with a feedforward action. Black color depicts blocks executed at current sampling rate. Red color depicts feedforward execution rate. Continuous-time domain is shown in blue. Signals n_i and n_v represent measurement noise for current and voltage sensing, respectively.

will be referred to as AD. The controller output, i.e., the reference voltage $v_{i,r}$, is processed by the digital pulsewidth modulator (DPWM), which outputs the transistor switching signal x with duty cycle D. The switching frequency is $f_{\text{pwm}} = 1/T_{\text{pwm}}$. Input dc bus voltage V_{in} is used for $v_{i,r}$ scaling [4].

A closed-loop block diagram of the current control system is shown in Fig. 1(b), where v_{pcc} is shown as a disturbance. The difference between the VSC output voltage v_i and v_{pcc} is applied to the output inductive filter

$$G_f(s) = \frac{i_L(s)}{v_i(s) - v_{\text{pcc}}(s)} = \frac{1}{sL} \tag{1}$$

where s is the complex variable of the Laplace transform and L is the inductance value. The resulting current i_L is sampled by an analog-to-digital converter (ADC) with a rate $f_s = N f_{\text{pwm}}$, where N is the multisampling (oversampling) factor. The frequency f_s will be referred to as the sampling and control frequency, and its inverse $T_s = 1/f_s$ as the control period. Values $N = \{1, 2\}$ correspond to uniformly single-sampled (SS-PWM) and double-sampled (DS-PWM) control [4], respectively. For $N > 2$, MS-PWM control loop is formed [38]. The control frequency determines the execution rate of the controller $G_c(z)$, where z is the Z-domain variable corresponding to T_s. Owing to finite algorithm computation time, the controller output is often delayed by one control period [4]. The control system in Fig. 1(b) also includes the AD block $H_{\text{ad}}(z_1)$ [16]. The execution rate of the AD block is independently chosen as $f_{s,1} = N_{\text{ad}} f_{\text{pwm}}$, where N_{ad} will be referred to as the AD oversampling factor. The Z-domain variable z_1 corresponds to $T_{s,1} = 1/f_{s,1}$. In case $f_{s,1} \neq f_s$, a rate conversion needs to be included after H_{ad}.

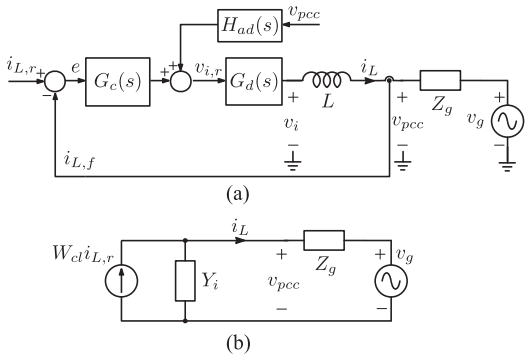

Fig. 2. S-domain representation of a grid-following VSC. (a) Current control system and grid connection. (b) Norton equivalent circuit used for impedance-based stability assessment.

A. S-Domain Representation of the Control System

In this article, modeling is performed in the s-domain to allow the investigation of VSC admittance properties even above the NF [27]. The impact of sidebands [18], [27], [34]–[36], [56] is not considered as it introduces additional complexity, without being crucial for the conclusions drawn in this article. The s-domain representation of the system is shown in Fig. 2(a). All time delays are represented by a unique block $G_d(s)$.

The triangular carrier is chosen for the DPWM [4]. Its small-signal model is obtained using the describing function approach [57]

$$G_{\text{dpwm}}(s) = \frac{d(s)}{m(s)} = \frac{1}{2}\left(e^{-sDT_s} + e^{-s(1-D)T_s}\right) \tag{2}$$

where m is the modulating waveform, equal to $v_{i,r}$ after one-step delay, and d is the continuous-time duty cycle of x, used in averaged modeling [4]. For $D = 0.5$, the DPWM model reduces to a pure time delay $e^{-s\frac{T_s}{2}}$. As this D is the mean value of duty cycles for sinusoidal ac operation, it will be used for the subsequent analysis. Together with one-step delay added due to algorithm execution time [4], the total time delay in the digital current control system is equal to

$$G_d(s) = \frac{v_i(s)}{v_{i,r}(s)} \approx e^{-s\tau_D} = e^{-s\frac{3}{2}T_s} = e^{-s\frac{3}{2}\frac{T_{\text{pwm}}}{N}}. \tag{3}$$

As a standard approach for sinusoidal reference tracking, the proportional–resonant (PR) controller is used in this article [4]

$$G_c(s) = k_p + k_r\frac{s}{s^2+\omega_1^2} \tag{4}$$

where k_p and k_r are the proportional and resonant gains, respectively, and ω_1 is the angular frequency of the current reference. As an example considered in this article, the proportional gain is chosen as $k_p = \omega_c L$, where ω_c is the sought angular crossover frequency of the current loop [4]. The resonant gain is chosen as $k_r = \frac{1}{10}\omega_c k_p$, which limits its impact to lower frequencies [4]. The value of ω_c relative to the angular switching frequency ω_{pwm}, labeled as $\alpha = \omega_c/\omega_{\text{pwm}}$, will be referred to as the relative bandwidth. The value of α is limited by system delays and PWM carrier frequency [4], [58].

B. Impedance-Based Stability

The impedance-based stability assessment requires representing the VSC with its Norton equivalent circuit, as in Fig. 2(b). The Norton current source determines the short-circuit current of the VSC, i.e., the value of i_L when $v_{\text{pcc}} = 0$

$$W_{\text{cl}}(s) = \left.\frac{i_L(s)}{i_{L,r}(s)}\right|_{v_{\text{pcc}}=0} = \frac{W_{\text{ol}}(s)}{1+W_{\text{ol}}(s)} \tag{5}$$

where $W_{\text{ol}}(s) = G_c(s)G_d(s)G_f(s)$ is the open-loop gain of the corresponding system. The input admittance Y_i is found as the inductor current response to the voltage v_{pcc} when current reference is set to 0

$$Y_i(s) = -\left.\frac{i_L(s)}{v_{\text{pcc}}(s)}\right|_{i_{L,r}=0} = \frac{G_f(s)(1-H_{\text{ad}}(s)G_d(s))}{1+W_{\text{ol}}(s)}. \tag{6}$$

From (6), it can be seen that the VSC input admittance is shaped by the output filter and the current control system, which includes digital delays and, if implemented, AD. The impact of outer loops on admittance is not modeled, as this article focuses on properties at frequencies significantly above their bandwidth [5].

Considering the VSC connection to a nonideal grid, i.e., $Z_g \neq 0$, the inductor current can be calculated using the equivalent circuit parameters as

$$i_L(s) = \frac{W_{\text{cl}}(s)}{1+Y_i(s)Z_g(s)}i_{L,r}(s) - \frac{Y_i(s)}{1+Y_i(s)Z_g(s)}v_g(s). \tag{7}$$

Assuming that W_{cl} is stable, the stability of the grid-connected VSC depends on the product $Y_i(s)Z_g(s)$, which is referred to as the minor-loop gain [29]. Stability analysis can be performed by applying the Nyquist stability criterion to the minor-loop gain.[1]

The input admittance Y_i is said to be passive if its phase is in the range $(-\frac{\pi}{2}, \frac{\pi}{2})$, i.e., if its real part is greater than or equal to 0 [5]. Imposing the requirement for passive Y_i, such as in [59], arises from the fact that if both Y_i and Z_g are passive, the phase of their product never crosses $\pm\pi$. Therefore, minor-loop gain always satisfies the Nyquist criterion.

Instead, a negative real part of Y_i determines nonpassive regions. For a control system described by (3) and (4), without AD, $\text{Re}\{Y_i(j\omega)\}$ first turns negative above $\omega \approx 2\pi\frac{f_s}{6}$ and its peak negative value is increased with higher ω_c and τ_d, and lower L [54].

[1]The admittance Y_i in (6) is the so-called single-frequency model [18], [27], [56]. The impact of sampling and modulation sideband components can be taken into account using multifrequency modeling [18], [27], [56]. It is important to note that the multifrequency model is by itself nonlinear; hence, using control tools derived for linear systems, such as the Nyquist stability criterion, is not strictly accurate. It will be shown that single-frequency Y_i models well the VSC behavior in the frequency range of interest. Consequently, linear analysis will be used to predict the stability of the grid-connected operation.

TABLE I
VSC AND CONTROL PARAMETERS

Description	label	value	unit
Nominal power	S_n	3	kVA
Nominal input voltage	V_{in}	400	V
Nominal PCC voltage	$v_{\text{pcc, RMS}}$	230	V
Fundamental frequency	f_1	50	Hz
Switching frequency	f_{pwn}	20	kHz
Filter inductance	L	$\{1.5, 2.5\}$	mH
Dead time	t_{dt}	500	ns

III. Analysis and Experimental Verification of Admittance Properties

A. Experimental Setup and Admittance Measurements for DS-PWM Without AD

For experimental admittance measurements and subsequent grid-connected tests, an industrial full-bridge VSC, described in Table I, is used. The VSC is operated using the bipolar modulation. Input voltage is provided by the regenerative power system Keysight RP7962A.

The control system is implemented on an NI sbRIO-9606, which is based on a Xilinix Zynq 7020 all programmable system on chip (AP-SoC). The controller is discretized using the impulse-invariant approach [4]. For all subsequent admittance measurements, $L = 1.5$ mH and $\alpha = 0.2$. For strategies other than MS-PWM, current is sampled and the control algorithm is executed twice per switching period, i.e., DS-PWM is used. Sampling instants coincide with peaks and valleys of the carrier [4].

Input admittance Y_i is measured by injecting voltage perturbation components at the PCC and measuring the current response, as in [54]. The perturbation voltage is generated using a power operational amplifier MP118 from APEX. Measurements are performed for 23 frequencies, one at a time, from 5 to 41 kHz, which is just above f_s for $N = 2$. Perturbation voltage is calculated to obtain, at least, 100 mA of perturbation component of i_L, to provide a good measurement resolution. A Tektronix 5 series oscilloscope is used to acquire i_L and v_{pcc} with data length equal to 40 ms and sampling rate of 250 MS/s. Data are postprocessed in MATLAB by calculating the fast Fourier transform of $-i_L$ and v_{pcc} and determining the admittance, based on their ratio at the perturbation frequency. The same measurement approach, described in more detail, is used in [54]. All the admittance measurements shown in this article were conducted for $v_g = 0$, leaving only the perturbation voltage component at the PCC. This sets the steady-state operating point to $D = 0.5$, which is compliant with the previous analysis. It is interesting to note that measurements were also conducted for other steady-state values of D. It is found that, as D approaches extreme values, the nonpassive zone peaks become less emphasized, which can be predicted by including the full DPWM model (2). Therefore, for sinusoidal ac operation, the highest introduced negative damping is expected around zero crossings of v_g. An analysis of the impact of DPWM operating point dependence on admittance measurements can be found in [56].

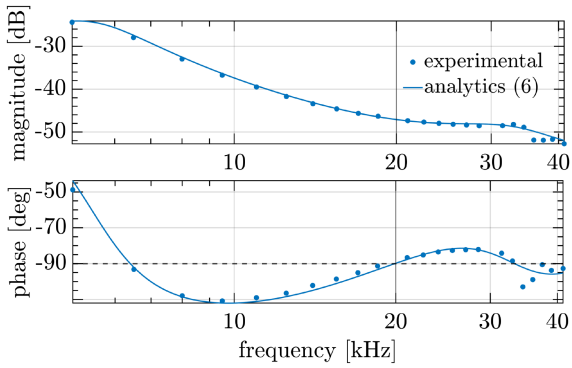

Fig. 3. Admittance measurements for the case of DS-PWM without AD: $N = 2$, $H_{ad} = 0$, $L = 1.5$ mH, $\alpha = 0.2$. The vertical line marks the switching (and the Nyquist) frequency.

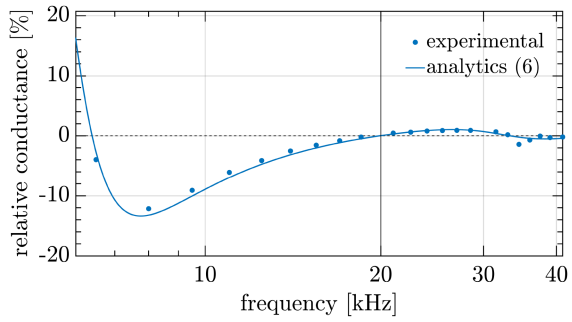

Fig. 4. Relative conductance for the case of DS-PWM without AD: $N = 2$, $H_{\text{ad}} = 0$, $L = 1.5$ mH, and $\alpha = 0.2$. The vertical line marks the switching (and the Nyquist) frequency.

As a benchmark, admittance measurements are given for the case of DS-PWM without AD. These results are shown in Fig. 3, where it can be seen that a very good match with analytics is obtained, even above the NF. At frequencies above $1.5f_{\text{pwm}}$, the single-frequency model starts to show a more significant mismatch, which is addressed in [56]. Note the existence of two nonpassive zones, where phase drops below $-90°$. The first one starts at approximately 6.5 kHz, which is consistent with the often mentioned critical frequency $f_s/6$ [16]. Another nonpassive zone appears above the NF. The goal of the passivity-based design, which is analyzed in the following subsections, is to suppress these nonpassive zones. As an additional illustration, the real part of measured Y_i, relative to the nominal VSC admittance $Y_n = \frac{S_n}{U_n^2} = 56.7$ mS, is shown in Fig. 4.

B. Impact of AD

The first method considered for comparison is D-AD [16], which extends passivity up to the NF by adding a derivative feedforward of v_{pcc} to the controller output, $H_{\text{ad}}(s) = sk_{\text{ad}}$. AD gain is chosen to compensate for the sign change of the real part of the frequency response of (6) [16]

$$k_{\text{ad}} = \frac{4\tau_D^2}{\pi^2}\omega_c. \tag{8}$$

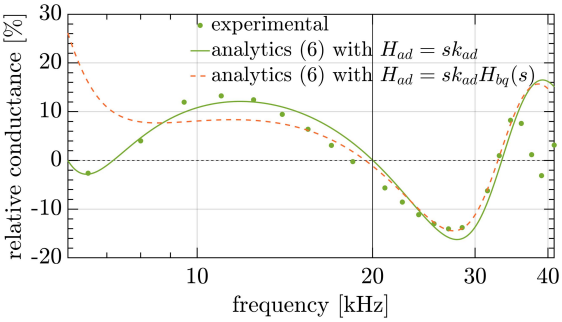

Fig. 5. Relative conductance for the case of D-AD: $N = 2$, $N_{\text{ad}} = 16$, $H_{\text{ad}} = \frac{k_{ad}}{T_{s,1}}(1 - z_1^{-1})$, $L = 1.5$ mH, and $\alpha = 0.2$. The vertical line marks the switching (and the Nyquist) frequency. Orange-dashed line shows the impact of including an additional filter H_{bq} in cascade with the derivative gain [16].

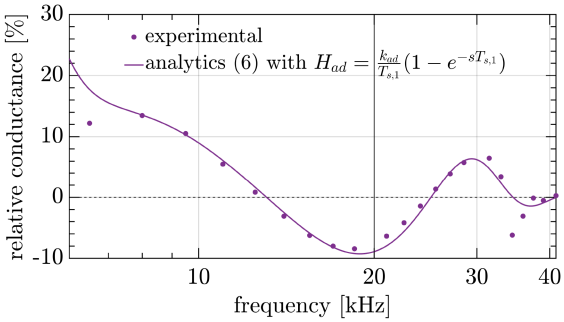

Fig. 6. Relative conductance for the case of DD-AD: $N = 2$, $N_{\text{ad}} = 2$, $H_{\text{ad}} = \frac{k_{ad}}{T_{s,1}}(1 - z_1^{-1})$, $L = 1.5$ mH, and $\alpha = 0.2$. The vertical line marks the switching (and the Nyquist) frequency.

In [16], it is shown that the derivative action must be implemented in the analog domain or using oversampling. The latter approach is chosen in this article in order to keep the implementation fully digital. Backward Euler discretization is chosen, as advised in [16]. Referring to Fig. 1(b), D-AD is implemented with $N = 2$, $N_{\text{ad}} = 16$, and $H_{\text{ad}}(z_1) = k_{\text{ad}} f_{s,1}(1 - z_1^{-1})$. The AD oversampling factor was chosen to be as high as allowed by the control platform. The relative value of the measured conductance for D-AD is shown in Fig. 5. A very good match with s-domain analytics is obtained, apart for frequencies very close to f_s. It is assumed that this mismatch comes from not including the sideband effects [56]. Results in Fig. 5 confirm that D-AD is capable of improving passivity up to NF[2]. It can be seen that, above the NF, a nonpassive zone is introduced with a peak of negative conductance being slightly higher than for the case of DS-PWM without AD. In [21], this effect is mentioned; however, it is not thoroughly investigated in the literature, even if, from [27], it is clear that admittance properties above the NF need to be examined. D-AD was also tested for other values of k_{ad}; however, these results are not shown due to article length limitations. The trend is that higher values of k_{ad} add more positive damping in the frequency region from $f_s/6$ to the NF and more negative damping in the region above the NF, where the peak negative conductance is found. Lower values of k_{ad} decrease the peak negative conductance above the NF; however, passivity is not achieved around $f_s/6$.

The second AD method compared, DD-AD, uses the same derivative action as D-AD, however, without oversampling: $N = 2$, $N_{\text{ad}} = 2$, and $H_{\text{ad}}(z) = k_{\text{ad}} f_s(1 - z^{-1})$. DD-AD is applied in [17], with a specific parameter design procedure. However, it was verified that implementing derivative gain as (8) brings practically the same results, without needing to use one fixed value of bandwidth as in [17]. In [17], Z-domain modeling was used to predict DD-AD impact on admittance, which yielded a significant mismatch as frequencies approached the NF. Hence, in this article, H_{ad} is directly transformed to s-domain, using $z = e^{sT_s}$. Results are reported in Fig. 6. It can be seen that a good match between experiments and analytics is obtained, in the same frequency range as in Figs. 4 and 5. From Fig. 6, it can be seen that DD-AD improves passivity at medium frequencies; however, above approximately $f_s/3$, passivity is lost. The same frequency limit is reported in papers that use single-loop AD, by adding derivative gain to the controller structure [7]. Note that the peak of negative conductance for DD-AD is slightly reduced compared to the case of DS-PWM without AD.

C. Impact of MS-PWM

It has been recently shown that a suitable candidate for grid-connected converters is the MS-PWM control, where $N > 2$ and $H_{\text{ad}} = 0$ [54]. Instead of compensating digital delays, MS-PWM relies on reducing them by increasing the update rate of the controller output. The main advantage of MS-PWM, compared to other strategies for US-PWM delay reduction [60], [61], is that both delays, due to controller output update and digital modulation, are reduced [38]. With MS-PWM, switching ripple is introduced in the feedback. While removing the switching ripple is beneficial regarding modulator linearity [47], it strongly deteriorates dynamic improvements. The analysis of MS-PWM operation without ripple filtering can be found in [38], [46], [53], [54], and [58], and such an approach is considered in this article as well. Particularly, in [54], it is shown that the presence of switching ripple does not deteriorate the passivation effectiveness of MS-PWM. For conciseness of this article, important practical aspects of MS-PWM implementation are left out, but interested readers can find detailed information in the papers cited above.

In [54], a thorough investigation of MS-PWM impact on admittance properties is given, for many values of N. There, it is shown that MS-PWM expands the passive region of Y_i, without needing to resort to AD. For lower values of N, such as 4, a small nonpassive zone appears close to f_{pwm}; however, negative damping is greatly reduced compared to $N = 2$. Further increase in N strongly reduces the nonpassive zone so

[2]In [16], an additional biquad filter H_{bq} is added in cascade with the derivative action, which is referred to as the modified active damping (M-D-AD). This filter adds damping to the narrow nonpassive zone around $f_s/6$ that remains when only derivative H_{ad} is used. It is not included in this article as it lacks a standardized design procedure [19], and its impact above the NF is negligible. However, it is important to note that M-D-AD can fully passivize the admittance in this region. Analytical trace corresponding to M-D-AD is shown in Fig. 5. This trace was validated, but measurements are not shown for figure clarity.

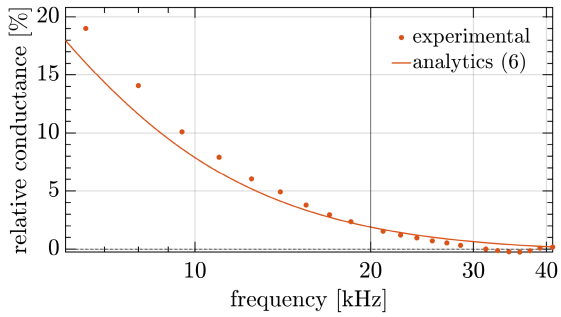

Fig. 7. Relative conductance for the case of MS-PWM: $N = 16$, $H_{\text{ad}} = 0$, $L = 1.5$ mH, and $\alpha = 0.2$. The vertical line marks the switching frequency.

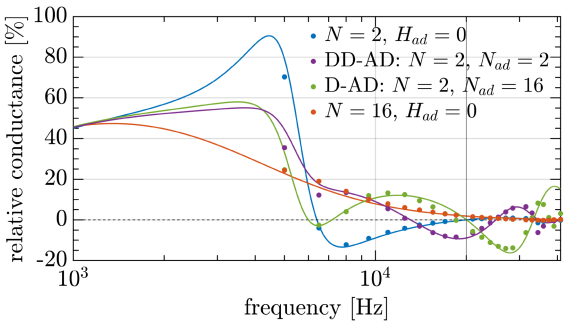

Fig. 8. Comparison of conductances for all tested control strategies: $L = 1.5$ mH, $\alpha = 0.2$. The vertical line marks the switching frequency.

that fully passive admittance is measured up to $1.5 f_{\text{pwm}}$ for $N > 8$ in [54]. As an example used for this article, admittance is measured for $N = 16$. The oversampling factor N is limited by the available processing power with respect to the switching frequency. Therefore, in the following section, $N = 4$ is also implemented to show that it is sufficient to retain the stability in the tested grid-connected operation. For the case of MS-PWM, the measured conductance is shown in Fig. 7. It can be seen that Y_i is almost fully passive, except for a very narrow range, where the conductance is just below 0.

D. Comparison of Effectiveness

In Fig. 8, conductances for all the tested cases are shown in an extended frequency range. It can be seen that both D-AD and DD-AD are able to extend the passive zone; however, for both the methods, another emphasized nonpassive zone is introduced, which is not present for the case of DS-PWM without AD. This points to the fact that the addition of AD only shifts the nonpassive zone to higher frequencies and can, therefore, compromise stability, instead of guaranteeing it. It is important to note that these nonpassive zones are found in the frequency range where single-frequency admittance models predict well the experimentally measured VSC responses. This is important as it can be assumed that assessing stability using the Nyquist criterion most likely yields correct conclusions, which is validated in the following section. MS-PWM shows a natural drop toward zero conductance, where Y_i starts to behave as an inductor. The summary of measured conductances is shown in Table II, by providing peaks of negative values and frequencies for which they are found. Results are also given for a second inductor with $L = 2.5$ mH. For MS-PWM, analytics predict the nonpassive zone to fall outside of the measurement range.

TABLE II
COMPARISON OF CONDUCTANCE MINIMUMS AND FREQUENCIES FOR WHICH THEY ARE FOUND: $\min\{R_e\{Y_i\}\}$ [%] @ $f_{\min}$ [kHz].

PWM	DS-PWM			MS-PWM
AD	w/o AD	D-AD	DD-AD	w/o AD
$L = 1.5$ mH				
exp.	−12.2 @ 8	−14.1 @ 27	−8.4 @ 18.5	−0.2 @ 36
analyt.	−13.4 @ 7.8	−16.2 @ 27.9	−9.3 @ 18.9	−0.1 @ 81
$L = 2.5$ mH				
exp.	−8.2 @ 8	−7.9 @ 27	−5 @ 18.5	−0.1 @ 36
analyt.	−8 @ 7.8	−9.7 @ 27.9	−5.6 @ 18.9	−0.05 @ 81

IV. Passivity Implications in Grid-Connected Scenarios

Impedance-based analysis from Section II-B predicts that a VSC can be destabilized if connected to a grid with a certain Z_g. For grid-following VSCs with inductive filters, a parallel antiresonance that coincides with the nonpassive zone of Y_i can cause instability [16]. In this section, operation stability is tested for all the strategies compared in Section III, by connecting the VSC to a grid with a specific Z_g. For all the results in this section, $L = 1.5$ mH and $\alpha = 0.2$. The results presented in this section hold, in relative terms, also for VSC designs with lower switching frequencies. Therefore, irrespective of the specific design parameters, reliable conclusions can be drawn on the robustness ensured by each controller organization.

A. Analysis of the Equivalent Impedance Network

Suppose that the analyzed VSC is connected to a grid with an antiresonance formed by L_g and C_g.[3] Grid passive damping can be modeled as a parallel conductance G_g. Such a grid impedance can, therefore, be described using its antiresonant frequency $f_{\text{res}} = \frac{\omega_{\text{res}}}{2\pi} = \frac{1}{2\pi\sqrt{L_g C_g}}$, characteristic impedance $Z_c = \sqrt{\frac{L_g}{C_g}}$, and quality factor $Q = \frac{1}{Z_c G_g}$. The analysis of passive damping is important, as a nonpassive Y_i does not necessarily destabilize the grid antiresonance with realistic values of Q [54].

In this section, VSC connection to three different grid antiresonances is tested. Antiresonant networks that coincide with nonpassive zones are formed using an inductor $L_g = 72$ μH and different parallel capacitors C_g. Passive damping of the antiresonant network was estimated from the exponential decay of oscillations triggered by imposing a transient while the VSC was disconnected. First antiresonance, $Z_{g,1}$, is obtained with $C_g = 5.6$ μF. It is very close to the peak of negative conductance for $N = 2$ without AD, and its parameters are $f_{\text{res}} = 7.9$ kHz,

[3]Note that specific L_g and C_g should not be understood as parts of a properly designed LCL filter, but as antiresonance forming components that may be found due to, for example, presence of grid-forming VSCs [23].

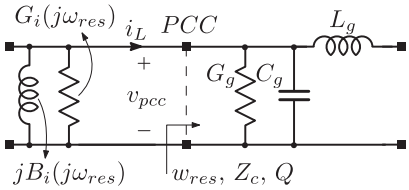

Fig. 9. Impedance network at the frequency of grid antiresonance. VSC admittance is represented as $Y_i(j\omega_{\text{res}}) = G_i(j\omega_{\text{res}}) + jB_i(j\omega_{\text{res}})$. Grid impedance features passive damping, represented by G_g.

$Q = 28$, $Z_c = 3.6\ \Omega$, and $G_g^{\%} = 17.6\%$. Second antiresonance, $Z_{g,2}$, is obtained with $C_g = 1\ \mu$F. It is very close to the peak of negative conductance for DD-AD, and its parameters are $f_{\text{res}} = 18.4$ kHz, $Q = 38$, $Z_c = 8.3\ \Omega$, and $G_g^{\%} = 5.6\%$. Third antiresonance, $Z_{g,3}$, is obtained with $C_g = 440$ nF. It is very close to the peak of negative conductance for D-AD, and its parameters are $f_{\text{res}} = 28.2$ kHz, $Q = 30$, $Z_c = 12.7\ \Omega$, and $G_g^{\%} = 4.6\%$.

The equivalent impedance network at the frequency of grid antiresonance is illustrated in Fig. 9. At ω_{res}, VSC input admittance is represented by its conductance $G_i(j\omega_{\text{res}})$ and susceptance $B_i(j\omega_{\text{res}})$. Intuitively, from Fig. 9, it can be concluded that overall system damping at ω_{res} is impacted by the parallel connection of $G_i(j\omega_{\text{res}})$ and G_g. Hence, the value of $G_i(j\omega_{\text{res}}) + G_g$ indicates the damping of the resonant network. This intuitive approach is valuable as it helps to predict the stability based solely on admittance measurements, without knowing the analytic expression for Y_i. A formal approach, in case Y_i is analytically known, is to analyze stability using Nyquist plots of the minor-loop gain. Examples of Nyquist plots, with analytic and measured data points, are shown in Fig. 10, for all the tested control strategies and grid impedances. From Fig. 10(a), it is clear that, although the antiresonance $Z_{g,1}$ coincides with the nonpassive zone of Y_i for DS-PWM without AD, grid passive damping is high enough to prevent instability. This can also be concluded from the fact that, for that case, $G_i(j\omega_{\text{res}}) + G_g > 0$. Nyquist plots in Fig. 10(b) and (c) predict instability for DD-AD and D-AD, respectively.

B. Experimental Grid-Connected Tests

The experimental prototype is the same used for admittance measurements. The grid is formed using Chroma 6460 programmable ac power supply and passive filters to form specific antiresonances. It was noticed that our Chroma was adding some damping at high frequencies; hence, it was decoupled with an additional LC filter with an antiresonant frequency equal to 650 Hz. This filter does not have direct implications on subsequent tests, and its purpose is to form an almost ideal voltage source at frequencies of interest. Voltage levels are reduced to $V_{\text{in}} = 250$ V and $v_{\text{pcc}} = 110$ V RMS to reduce any impact of unstable operation. The VSC operates as a rectifier with unity power factor, as our Chroma does not support regenerative operation.

Results of all grid-connected tests are shown in Fig. 11. The oscilloscope screen shows i_L (orange) and v_{pcc} (red). Each column of subfigures shows results for one grid antiresonance. In first two rows, results are shown for the case of MS-PWM with $N = 4$ and $N = 16$, which enable stable operation for all the tested antiresonances. Transient is tested by imposing a step reference change from 4 A to 15 A, at the peak of the fundamental component. Results for $N = 4$ are given to show that it is not always necessary to raise N to very high values. Note that, based on results from [54], MS-PWM with $N = 4$ results in a small nonpassive zone around f_{pwm}, which coincides with the antiresonance $Z_{g,2}$. However, introduced negative damping is strongly suppressed; hence, passive grid damping is enough to compensate it.

In the third row of Fig. 11, results are shown for DS-PWM strategies that feature nonpassive zones, which coincide with the correspondingly tested antiresonances. In Fig. 11(g), strong resonant oscillations are triggered; however, as predicted by Fig. 10(a), due to sufficiently high passive damping of $Z_{g,1}$, instability is prevented. In Fig. 11(h) and (i), instability occurs for AD strategies, as predicted by Fig. 10(b) and (c). For these antiresonances, DS-PWM without AD is stable; hence, results show transients when the respective AD strategy is activated. In Fig. 11(h), overvoltage protection is triggered when DD-AD is activated, and the VSC is turned OFF. In Fig. 11(i), when D-AD is activated, protection is not triggered; however, instability clearly occurs and the controller output jitters from positive to negative saturation limits. From Fig. 11(i), it is clear that oscillations are much more emphasized around zero crossings of v_{pcc}, where $D = 0.5$. This is in agreement with comments made in Section III-A regarding the impact of the operating point on the negative peak of Y_i. Note that this case corresponds to the instability caused by antiresonance above the NF. Its enabling mechanism is the coupling between sampling and modulation sidebands, which allows the controller to react to a disturbance above the NF [27]. In the fourth row of Fig. 11, zoomed waveforms corresponding to the third row are given to show that oscillations are triggered at the antiresonant frequency.

It can be concluded that the implementation of DS-PWM with AD may destabilize operation for certain grid antiresonances. Hence, AD *does not guarantee the stability* of a grid-connected VSC for any *passive* Z_g. On the other hand, MS-PWM retains stability for all the tested cases.

V. Analysis of Noise Sensitivity

A question that arises for AD strategies is their noise sensitivity [13], [54], as derivative action is applied to v_{pcc}. The goal of this section is to quantify the noise propagation from sensing to the output current i_L, for passivizing control strategies tested beforehand. As seen in Fig. 1(b), noise due to current measurement, n_i, is present for all the strategies, while AD brings an additional noise path to the system from n_v to i_L. A detailed analysis of noise propagation for dc–dc converters is given in [52], and the same approach and assumptions are taken in this article. It is assumed that n_i and n_v are wide-sense stationary Gaussian white noise signals [62], with corresponding variances labeled as σ_i^2 and σ_v^2. In this way, an analysis of the resulting output current variance $\sigma_{i_L}^2$ can be performed applying the theory of linear

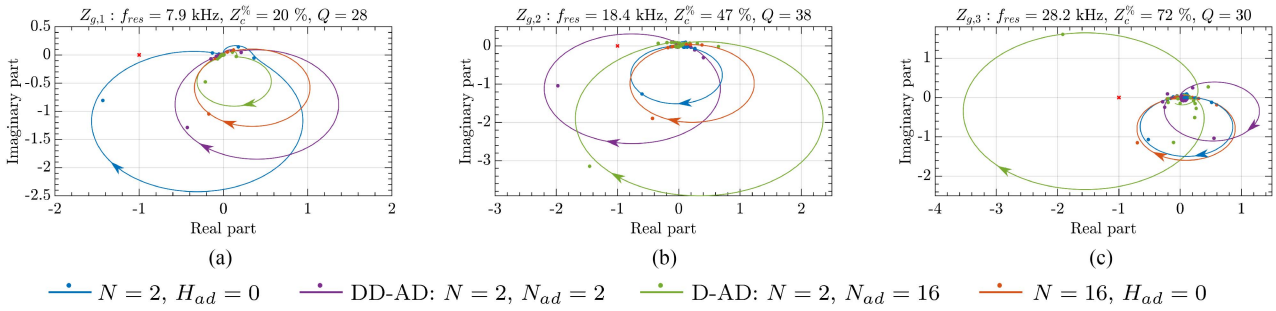

Fig. 10. Nyquist plots of the minor-loop gain $Y_i(j\omega)Z_g(j\omega)$ for three different grid antiresonances and all compared control strategies.

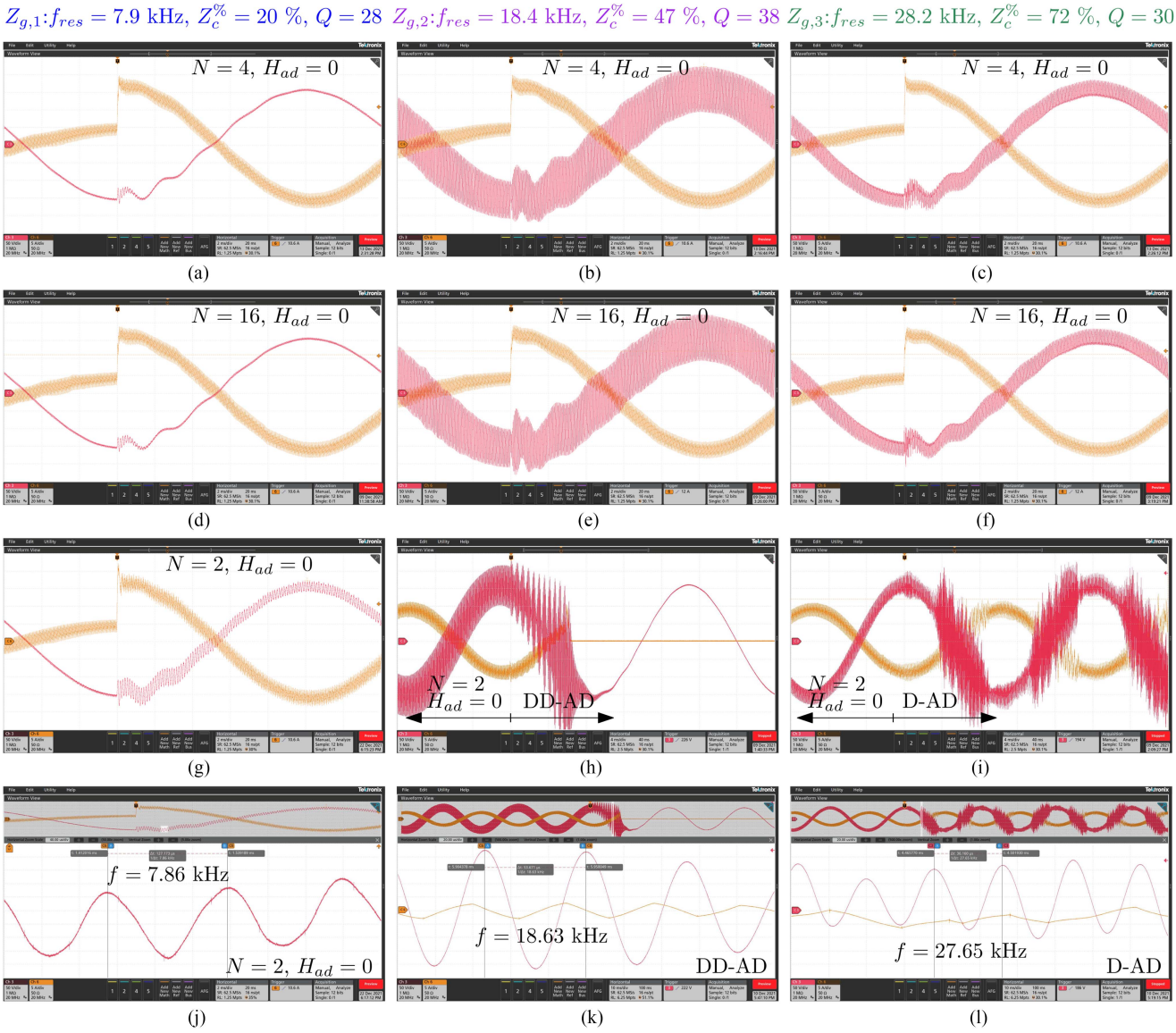

Fig. 11. Experimental demonstration of passivity implications in grid-connected scenarios. Orange line shows i_L and red line shows v_{pcc} that has variable ripple depending on C_g. Each column features results for different tested grid impedances Z_g. Grid impedances are formed as LC antiresonant circuits and feature certain passive damping. Results are shown as transient responses to step reference change for (a)–(c) MS-PWM with $N = 4$, (d)–(f) MS-PWM with $N = 16$, and (g) DS-PWM without AD with nonpassive zone of Y_i coinciding with $Z_{g,1}$ antiresonance; here, operation features strong oscillations at f_{res}, but passive grid damping prevents instability. (h) Operation change from DS-PWM without AD to DD-AD. Owing to weakly damped $Z_{g,2}$ antiresonance, coinciding with the nonpassive zone of Y_i, instability occurs and protection is triggered. (i) Operation change from DS-PWM without AD to D-AD. Owing to weakly damped $Z_{g,3}$ antiresonance, coinciding with the nonpassive zone of Y_i, instability occurs. (j)–(l) Zoomed waveforms from the row above, showing oscillation frequencies.

time-invariant discrete-time filtering of stochastic signals [42], [62].

For all the compared strategies, noise propagation due to n_i is determined by [62]

$$\sigma_{i_L}^2\big|_{n_v=0} = \int_0^{f_x} \sigma_i^2 \frac{2}{f_s}|H_{ni}(f)|^2 df = \int_0^{f_x} S_{ni}(f)df \quad (9)$$

where f_x is the band of interest, $|H_{ni}(f)|^2 = \frac{|W_{\text{ol}}(f)|^2}{|1+W_{\text{ol}}(f)|^2}$ is the squared magnitude response from n_i to i_L in Fig. 1(b), and $S_{ni}(f)$ is the noise power spectral density of the inductor current, caused by n_i. It can be seen that the spectral power density is decreased by oversampling the feedback, as determined by f_s. In [52], it is shown that analyzing noise using (9) provides a good prediction for SS-PWM and DS-PWM single-loop controllers. For the case of MS-PWM, it is shown that the limiting aspect is the fact that the triangular DPWM behaves as a resampler with frequency $2f_{\text{pwm}}$, thus causing aliasing of noise power above f_{pwm}. For this reason, digital antialiasing filters are needed to suppress the resulting noise floor below the level determined by DS-PWM [52].

For AD, noise propagation due to n_v is determined by

$$\sigma_{i_L}^2\big|_{n_i=0} = \int_0^{f_x} \sigma_v^2 \frac{2}{f_{s,1}}|H_{nv}(f)|^2 df = \int_0^{f_x} S_{nv}(f)df \quad (10)$$

where $|H_{nv}(f)|^2$ is the squared magnitude response from n_v to i_L and $S_{nv}(f)$ is the noise power spectral density of the inductor current, caused by n_v. Assuming that the two noise signals are uncorrelated, total in-band variance of i_L can be obtained as an algebraic sum of (9) and (10) [62].

An interesting fact is that, for the case of D-AD, white noise n_v is shaped by the AD filter before being sampled with f_s. In the case of digital implementation, this corresponds to decimation from $f_{s,1}$ to f_s. Let us, for this reason, define $|H_{nv}(f)|^2$ as a product of squared magnitude responses from n_v to the decimator output and from the decimator output to i_L

$$|H_{nv}(f)|^2 = |H_{\text{ad}}^{M:1}(f)|^2 \frac{|G_d(f)G_f(f)|^2}{|1+W_{\text{ol}}(f)|^2} \quad (11)$$

where $M = \frac{f_{s,1}}{f_s}$ is the decimation factor and $|H_{\text{ad}}^{M:1}(f)|^2$ is the modified squared magnitude response of the AD filter that includes the decimation impact. Given that n_v is a stationary white stochastic signal, it exhibits no spectral correlation and its power spectral density is constant [62], [63]. For this reason, to obtain the equivalent model valid for power spectral density analysis, it is possible to directly apply the expression for frequency-domain relation between the input and the output of a downsampler, assuming integer values of M [62], [63]

$$|H_{\text{ad}}^{M:1}(f)|^2 = \sum_{k=0}^{M-1} |H_{\text{ad}}(f - kf_s)|^2. \quad (12)$$

For the case of DD-AD, where $M = 1$, $|H_{\text{ad}}^{M:1}(f)|^2 = |H_{\text{ad}}(f)|^2$.

Individual impacts of (9) and (10) on the total variance of i_L for DS-PWM are illustrated in Fig. 12, by showing values of $S_n \in \{S_{ni}, S_{nv}\}$. Values of input noise powers, $\sigma_i^2 = 1.7 \times 10^{-3}$ A^2 and $\sigma_v^2 = 154 \times 10^{-3}$ V^2, are estimated from sampled i_L and v_{pcc}, obtained while the VSC was running in open-loop condition. It can be seen that, for DD-AD, spectral power density due to voltage noise sensing is well below the one due to current noise sensing; hence, voltage noise propagation is completely masked and $\sigma_{i_L}^2$ is expected to be the same as for DS-PWM without AD. This outcome is a result of a relatively low derivative gain k_{ad} (8). For D-AD, however, the derivative in H_{ad} first causes the amplification of the high-frequency noise content, which then gets decimated and folded back to frequencies below the NF. This causes the in-band noise power to significantly increase. From Fig. 12, it can be seen that for $N_{\text{ad}} = 16$, which is used in this article, spectral power densities due to n_i and n_v almost overlap. For $N_{\text{ad}} = 32$, n_v has a higher impact than n_i. Note that for the analog implementation of D-AD, $M \to \infty$ and the impact of n_v is even higher, with the exact amount being dependent on the actual bandwidth of the noise signal. These results may seem counterintuitive, stating that oversampling causes a higher resulting noise floor. However, they come from the fact that for D-AD, H_{ad} needed to render Y_i fully passive up to the NF does not include any antialiasing filters [16]. In cases where full passivity up to the NF is not crucial, an antialiasing filter can be placed between H_{ad} and the decimator, which would result in a strong noise suppression compared to DD-AD, while offering similar passivizing effectiveness. This requires additional investigation and is a potential topic of further research. Note that this effect is closely related to conclusions brought in [52], regarding DPWM decimation for MS-PWM with PID controllers. The impact of DPWM decimation is, however, more complex to analyze as it occurs inside the closed loop; hence, it is left for future research. It should be noted that results in Fig. 12 are directly proportional to given σ_i^2 and σ_v^2. Hence, for a higher ratio σ_v^2/σ_i^2, D-AD can show an increased sensitivity even for lower values of N_{ad}. However, regarding DD-AD, spectral power density line for n_v stays more than 20 dBA^2/Hz below the one for n_i, meaning that σ_v^2 should increase more than 100 times to result in a comparable impact, which is not a realistic case. Hence, it can be concluded that DD-AD is not likely to be prone to noise sensitivity.

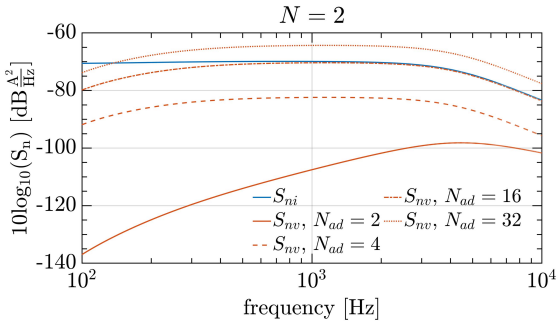

Fig. 12. Noise power spectral densities ($S_n \in \{S_{ni}, S_{nv}\}$) of i_L for DS-PWM due to current noise sensing (blue trace) and voltage noise sensing (red traces). Presented results are calculated for $L = 2.5$ mH, $\alpha = 0.1$, $\sigma_i^2 = 1.7 \times 10^{-3}$ A^2, and $\sigma_v^2 = 154 \times 10^{-3}$ V^2.

For experimental verification, reference current is set to 5 A RMS and $L = 2.5$ mH is used in order to capture the current

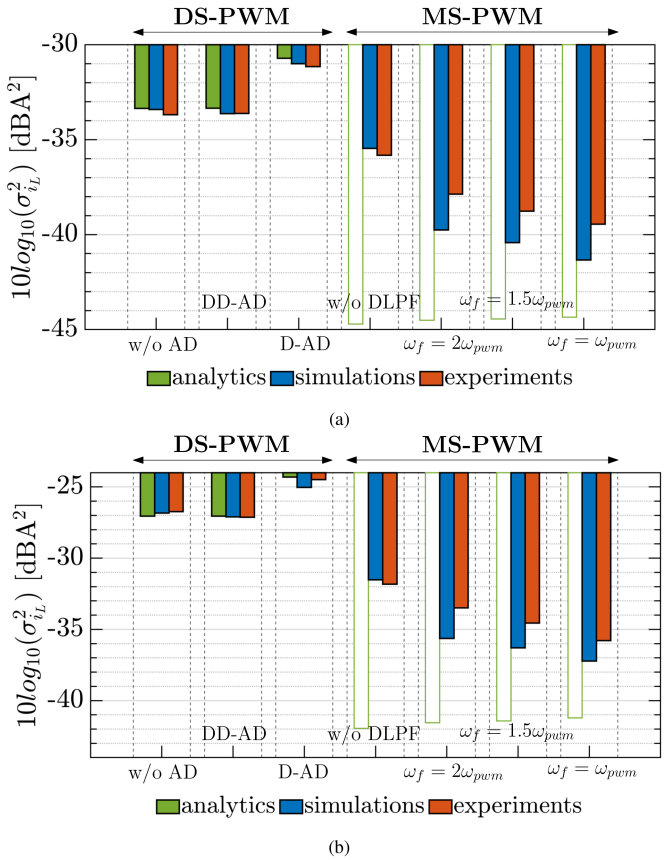

Fig. 13. Variance of i_L up to $f_{\text{pwm}}/2$ for $L = 2.5$ mH and (a) $\alpha = 0.1$ and (b) $\alpha = 0.2$.

signal using oscilloscope with 2 A/div scale. Larger scale was resulting in noise floor of the oscilloscope compromising i_L noise measurements. Output variance, up to $f_{\text{pwm}}/2$, is calculated in MATLAB using 200 ms of oscilloscope data sampled with 250 MS/s. Fundamental component and its harmonics are removed, so that distortion does not impact variance calculations. As a benchmark, simulations are implemented in Simulink using PLECS Blockset, as in [52]. White noise signals are injected, with variances corresponding to measured σ_i^2 and σ_v^2.

Results that show variance $\sigma^2_{i_L}$ for all the tested strategies are given in Fig. 13. Experimental measurements are compared with simulations and analytics. Results in Fig. 13(a) are given for relative bandwidth $\alpha = 0.1$. First, it can be seen that an excellent analytic prediction is obtained for DS-PWM without AD and DD-AD. Results show almost the same output noise power for these two strategies. As both the cases feature the same magnitude response $|H_{ni}|$, it is concluded that the voltage noise propagation for DD-AD is completely masked by the stronger current noise propagation, which is consistent with Fig. 12. For D-AD, analytics predict 2.6 dBA^2 noise power increase, while simulations and experiments show approximately 2.4 dBA^2 and 2.5 dBA^2 increase, respectively, which supports the validity of the model (12). As discussed above, for setups that feature a higher ratio σ_v^2/σ_i^2, higher noise sensitivity of D-AD is expected. Equation (9) predicts that, compared to DS-PWM, implementing MS-PWM with $N = 16$ would decrease the output noise power by, at least, a factor 8. The exact amount depends on the impact of delay reduction on $|H_{ni}|$. However, as analyzed in [52], for $N > 2$ and controllers with a nearly constant high-frequency gain, the power spectral density remains almost unaffected due to aliasing caused by DPWM resampling effects; hence, additional high-frequency digital filtering is needed to enable a strong in-band noise suppression. For this article, three digital low-pass filters (DLPFs) are tested to observe their impact on noise attenuation. DLPFs are implemented as first-order filters with cutoff frequencies $\omega_f = \{2, 1.5, 1\} \cdot \omega_{\text{pwm}}$ and are discretized using the bilinear transform. It is important to notice that these DLPFs do not directly attenuate noise power in the observed frequency window. The design goal is to suppress noise power above f_{pwm} with as little impact on dynamic performance.[4] DLPFs with lower cutoff frequencies bring more filtering at $f > f_{\text{pwm}}$; hence, corresponding results are expected to approach the value determined by (9). This trend is confirmed by results in Fig. 13(a), where the analytic prediction is only outlined as it does not model the impact of DPWM decimation. Again, simulations are in a good match with experiments. Note that, even without DLPF, noise power is reduced compared to DS-PWM without AD by 2.2 dBA^2, due to a higher phase margin, which brings additional filtering by $|H_{ni}|$.

Same conclusions are brought based on results shown in Fig. 13(b), given for $\alpha = 0.2$, except that all variances are increased due to the higher bandwidth setting. It can also be seen that a higher noise suppression of MS-PWM without DLPF relative to DS-PWM without AD is obtained, equal to approximately 5 dBA^2, due to a higher phase margin difference between the two. Finally, compared to $\alpha = 0.1$, for MS-PWM, there is a bigger mismatch between measured noise power and the analytic prediction that does not consider DPWM resampling effects. This is explained by the fact that the increased proportional gain results in a higher amplification of noise power above f_{pwm}, which gets decimated by the DPWM. Hence, same digital filters become less effective in suppressing the aliasing impact.

The main conclusion of this section is that implementing AD does not necessarily result in excessive noise sensitivity. Still, MS-PWM is able to offer additional noise suppression without compromising the passivation effectiveness.

VI. Conclusion

This article has provided a comparison in the effectiveness and noise sensitivity of control strategies used to render the input admittance of grid-connected VSCs passive. MS-PWM was compared against typically used derivative-based AD methods. It was shown that MS-PWM outperforms AD in terms of effectiveness, as AD brings a negative impact around and above the NF. Grid-connected operation was tested for different antiresonances, and it was shown that only MS-PWM enables robust stability. Analytic modeling of noise propagation

[4]In order to verify that implemented DLPFs do not strongly deteriorate passivity properties, admittances are measured for tested DLPFs and only a small impact is seen. Peaks of negative conductance, measured for $\alpha = 0.2$ for compatibility with results in Table II, are $\{-0.25, -0.17\}\%$ for $L = \{1.5, 2.5\}$ mH at 28 kHz.

was developed, and it was shown that AD strategies are not highly sensitive. Still, MS-PWM outperforms AD in this respect as well. The study shown in this article further pointed out that MS-PWM is a very viable solution for achieving high bandwidths, while guaranteeing stability of current-controlled grid-connected VSCs.

REFERENCES

[1] F. Blaabjerg, R. Teodorescu, M. Liserre, and A. Timbus, "Overview of control and grid synchronization for distributed power generation systems," *IEEE Trans. Ind. Electron.*, vol. 53, no. 5, pp. 1398–1409, Oct. 2006.

[2] D. Boroyevich, I. Cvetkovic, R. Burgos, and D. Dong, "Intergrid: A future electronic energy network?," *IEEE Trans. Emerg. Sel. Topics Power Electron.*, vol. 1, no. 3, pp. 127–138, Sep. 2013.

[3] X. Wang and F. Blaabjerg, "Harmonic stability in power electronic-based power systems: Concept, modeling, and analysis," *IEEE Trans. Smart Grid*, vol. 10, no. 3, pp. 2858–2870, May 2019.

[4] S. Buso and P. Mattavelli, *Digital Control in Power Electronics* (ser. Synthesis Lectures on Power Electronics), 2nd ed. San Rafael, CA, USA: Morgan & Claypool, 2015.

[5] L. Harnefors, X. Wang, A. G. Yepes, and F. Blaabjerg, "Passivity-based stability assessment of grid-connected VSCs—An overview," *IEEE Trans. Emerg. Sel. Topics Power Electron.*, vol. 4, no. 1, pp. 116–125, Mar. 2016.

[6] J. Dannehl, M. Liserre, and F. W. Fuchs, "Filter-based active damping of voltage source converters with *lcl* filter," *IEEE Trans. Ind. Electron.*, vol. 58, no. 8, pp. 3623–3633, Aug. 2011.

[7] X. Wang, F. Blaabjerg, and P. C. Loh, "Passivity-based stability analysis and damping injection for multiparalleled VSCs with LCL filters," *IEEE Trans. Power Electron.*, vol. 32, no. 11, pp. 8922–8935, Nov. 2017.

[8] W. Yao, Y. Yang, Y. Xu, F. Blaabjerg, S. Liu, and G. Wilson, "Phase reshaping via all-pass filters for robust LCL-filter active damping," *IEEE Trans. Power Electron.*, vol. 35, no. 3, pp. 3114–3126, Mar. 2020.

[9] A. Akhavan, J. C. Vasquez, and J. M. Guerrero, "A simple method for passivity enhancement of current controlled grid-connected inverters," *IEEE Trans. Power Electron.*, vol. 35, no. 8, pp. 7735–7741, Aug. 2020.

[10] A. Akhavan, H. R. Mohammadi, J. C. Vasquez, and J. M. Guerrero, "Passivity-based design of plug-and-play current-controlled grid-connected inverters," *IEEE Trans. Power Electron.*, vol. 35, no. 2, pp. 2135–2150, Feb. 2020.

[11] C. Xie, K. Li, J. Zou, and J. M. Guerrero, "Passivity-based stabilization of LCL-type grid-connected inverters via a general admittance model," *IEEE Trans. Power Electron.*, vol. 35, no. 6, pp. 6636–6648, Jun. 2020.

[12] S. Li and H. Lin, "A capacitor-current-feedback positive active damping control strategy for LCL-type grid-connected inverter to achieve high robustness," *IEEE Trans. Power Electron.*, vol. 37, no. 6, pp. 6462–6474, Jun. 2022.

[13] M. A. Awal, L. D. Flora, and I. Husain, "Observer based generalized active damping for voltage source converters with LCL filters," *IEEE Trans. Power Electron.*, vol. 37, no. 1, pp. 125–136, Jan. 2022.

[14] L. Yang *et al.*, "Robust active damping control for LCL-type shunt active power filters," *IEEE Access*, vol. 10, pp. 39456–39 470, 2022.

[15] X. Wang, Y. He, D. Pan, H. Zhang, Y. Ma, and X. Ruan, "Passivity enhancement for LCL-filtered inverter with grid current control and capacitor current active damping," *IEEE Trans. Power Electron.*, vol. 37, no. 4, pp. 3801–3812, Apr. 2022.

[16] L. Harnefors, A. G. Yepes, A. Vidal, and J. Doval-Gandoy, "Passivity-based controller design of grid-connected VSCs for prevention of electrical resonance instability," *IEEE Trans. Ind. Electron.*, vol. 62, no. 2, pp. 702–710, Feb. 2015.

[17] E. Rodriguez-Diaz, F. D. Freijedo, J. M. Guerrero, J.-A. Marrero-Sosa, and D. Dujic, "Input-admittance passivity compliance for grid-connected converters with an LCL filter," *IEEE Trans. Ind. Electron.*, vol. 66, no. 2, pp. 1089–1097, Feb. 2019.

[18] F. D. Freijedo, M. Ferrer, and D. Dujic, "Multivariable high-frequency input-admittance of grid-connected converters: Modeling, validation, and implications on stability," *IEEE Trans. Ind. Electron.*, vol. 66, no. 8, pp. 6505–6515, Aug. 2019.

[19] F. Hans, W. Schumacher, S.-F. Chou, and X. Wang, "Passivation of current-controlled grid-connected VSCs using passivity indices," *IEEE Trans. Ind. Electron.*, vol. 66, no. 11, pp. 8971–8980, Nov. 2019.

[20] H. Yu, M. A. Awal, H. Tu, Y. Du, S. Lukic, and I. Husain, "Passivity-oriented discrete-time voltage controller design for grid-forming inverters," in *Proc. IEEE Energy Convers. Congr. Expo.*, 2019, pp. 469–475.

[21] H. Wu and X. Wang, "Virtual-flux-based passivation of current control for grid-connected VSCs," *IEEE Trans. Power Electron.*, vol. 35, no. 12, pp. 12673–12677, Dec. 2020.

[22] M. A. Awal, W. Yu, and I. Husain, "Passivity-based predictive-resonant current control for resonance damping in LCL-equipped VSCs," *IEEE Trans. Ind. Appl.*, vol. 56, no. 2, pp. 1702–1713, Mar./Apr. 2020.

[23] Y. Liao, X. Wang, and F. Blaabjerg, "Passivity-based analysis and design of linear voltage controllers for voltage-source converters," *IEEE Open J. Ind. Electron. Soc.*, vol. 1, pp. 114–126, 2020.

[24] J. Serrano-Delgado, S. Cobreces, M. Rizo, and E. J. Bueno, "Low-order passivity-based robust current control design for grid-tied VSCs," *IEEE Trans. Power Electron.*, vol. 36, no. 10, pp. 11886–11899, Oct. 2021.

[25] Z. Yang, C. Shah, T. Chen, J. Teichrib, and R. W. De Doncker, "Virtual damping control design of three-phase grid-tied PV inverters for passivity enhancement," *IEEE Trans. Power Electron.*, vol. 36, no. 6, pp. 6251–6264, Jun. 2021.

[26] J. Zhao, C. Xie, K. Li, J. Zou, and J. M. Guerrero, "Passivity-oriented design of LCL-type grid-connected inverters with Luenberger observer-based active damping," *IEEE Trans. Power Electron.*, vol. 37, no. 3, pp. 2625–2635, Mar. 2022.

[27] L. Harnefors, R. Finger, X. Wang, H. Bai, and F. Blaabjerg, "VSC input-admittance modeling and analysis above the Nyquist frequency for passivity-based stability assessment," *IEEE Trans. Ind. Electron.*, vol. 64, no. 8, pp. 6362–6370, Aug. 2017.

[28] R. Middlebrook, "Input filter considerations in design and application of switching regulators," in *Proc. IEEE Ind. Appl. Soc. Annu. Meeting*, Oct. 1976, pp. 366–382.

[29] J. Sun, "Impedance-based stability criterion for grid-connected inverters," *IEEE Trans. Power Electron.*, vol. 26, no. 11, pp. 3075–3078, Nov. 2011.

[30] B. Wen, D. Dong, D. Boroyevich, R. Burgos, P. Mattavelli, and Z. Shen, "Impedance-based analysis of grid-synchronization stability for three-phase paralleled converters," *IEEE Trans. Power Electron.*, vol. 31, no. 1, pp. 26–38, Jan. 2016.

[31] X. Wang, L. Harnefors, and F. Blaabjerg, "Unified impedance model of grid-connected voltage-source converters," *IEEE Trans. Power Electron.*, vol. 33, no. 2, pp. 1775–1787, Feb. 2018.

[32] X. Wang, F. Blaabjerg, and W. Wu, "Modeling and analysis of harmonic stability in an ac power-electronics-based power system," *IEEE Trans. Power Electron.*, vol. 29, no. 12, pp. 6421–6432, Dec. 2014.

[33] X. Yue, F. Zhuo, S. Yang, Y. Pei, and H. Yi, "A matrix-based multifrequency output impedance model for beat frequency oscillation analysis in distributed power systems," *IEEE Trans. Emerg. Sel. Topics Power Electron.*, vol. 4, no. 1, pp. 80–92, Mar. 2016.

[34] D. Yang, X. Wang, and F. Blaabjerg, "Sideband harmonic instability of paralleled inverters with asynchronous carriers," *IEEE Trans. Power Electron.*, vol. 33, no. 6, pp. 4571–4577, Jun. 2018.

[35] V. Pirsto, J. Kukkola, M. Hinkkanen, and L. Harnefors, "Intersample modeling of the converter output admittance," *IEEE Trans. Ind. Electron.*, vol. 68, no. 11, pp. 11348–11358, Nov. 2021.

[36] Q. Liu, Y. Ying, and M. Wu, "Extended harmonic resonance analysis of grid-connected converters considering the frequency coupling effect," *IEEE Trans. Ind. Electron.*, vol. 69, no. 9, pp. 9353–9363, Sep. 2022.

[37] G. Walker, "Digitally-implemented naturally sampled PWM suitable for multilevel converter control," *IEEE Trans. Power Electron.*, vol. 18, no. 6, pp. 1322–1329, Nov. 2003.

[38] L. Corradini and P. Mattavelli, "Modeling of multi-sampled pulse width modulators for digitally controlled dc-dc converters," *IEEE Trans. Power Electron.*, vol. 23, no. 4, pp. 1839–1847, Jul. 2008.

[39] L. Corradini, W. Stefanutti, and P. Mattavelli, "Analysis of multi-sampled current control for active filters," *IEEE Trans. Ind. Appl.*, vol. 44, no. 6, pp. 1785–1794, Nov./Dec. 2008.

[40] L. Corradini, P. Mattavelli, E. Tedeschi, and D. Trevisan, "High-bandwidth multi-sampled digitally controlled dc–dc converters using ripple compensation," *IEEE Trans. Ind. Electron.*, vol. 55, no. 4, pp. 1501–1508, Apr. 2008.

[41] X. Zhang, P. Chen, C. Yu, F. Li, H. T. Do, and R. Cao, "Study of a current control strategy based on multisampling for high-power grid-connected inverters with an LCL filter," *IEEE Trans. Power Electron.*, vol. 32, no. 7, pp. 5023–5034, Jul. 2017.

[42] J. Yang, J. Liu, J. Zhang, N. Zhao, Y. Wang, and T. Q. Zheng, "Multirate digital signal processing and noise suppression for dual active bridge dc–dc converters in a power electronic traction transformer," *IEEE Trans. Power Electron.*, vol. 33, no. 12, pp. 10885–10902, Dec. 2018.

[43] J. Yang *et al.*, "Carrier-based digital PWM and multirate technique of a cascaded H-bridge converter for power electronic traction transformers," *IEEE Trans. Emerg. Sel. Topics Power Electron.*, vol. 7, no. 2, pp. 1207–1223, Jun. 2019.

[44] C. Restrepo, T. Konjedic, F. Flores-Bahamonde, E. Vidal-Idiarte, J. Calvente, and R. Giral, "Multi-sampled digital average current controls of the versatile buck-boost converter," *IEEE Trans. Emerg. Sel. Topics Power Electron.*, vol. 7, no. 2, pp. 879–890, Jun. 2019.
[45] J. Ma, X. Wang, F. Blaabjerg, W. Song, S. Wang, and T. Liu, "Multisampling method for single-phase grid-connected cascaded H-bridge inverters," *IEEE Trans. Ind. Electron.*, vol. 67, no. 10, pp. 8322–8334, Oct. 2020.
[46] Z. Zhou, J. Wang, Z. Liu, and J. Liu, "Accurate prediction of vertical crossings for multi-sampled digital-controlled buck converters," in *Proc. IEEE Appl. Power Electron. Conf. Expo.*, 2020, pp. 292–298.
[47] S. He, D. Zhou, X. Wang, and F. Blaabjerg, "Aliasing suppression of multi-sampled current controlled LCL-filtered inverters," *IEEE Trans. Emerg. Sel. Topics Power Electron.*, vol. 10, no. 2, pp. 2411–2423, Apr. 2021.
[48] S. He, D. Zhou, X. Wang, and F. Blaabjerg, "Multisampling based grid impedance estimation for two-cell interleaved three-phase inverters," in *Proc. IEEE Energy Convers. Congr. Expo.*, 2021, pp. 590–594.
[49] S. He, D. Zhou, X. Wang, and F. Blaabjerg, "Line voltage sensorless control of grid-connected inverters using multisampling," *IEEE Trans. Power Electron.*, vol. 37, no. 4, pp. 4792–4803, Apr. 2022.
[50] I. Z. Petric, P. Mattavelli, and S. Buso, "A jitter amplification phenomenon in multi-sampled digital control of power converters," *IEEE Trans. Power Electron.*, vol. 36, no. 8, pp. 8685–8695, Aug. 2021.
[51] I. Petric, R. Cvetanovic, P. Mattavelli, S. Buso, and S. Vukosavic, "Analysis and DSP implementation of multi-sampled three-phase current controllers," in *Proc. 21st Int. Symp. Power Electron.*, 2021, pp. 1–7.
[52] I. Z. Petric, P. Mattavelli, and S. Buso, "Feedback noise propagation in multi-sampled dc–dc power electronic converters," *IEEE Trans. Power Electron.*, vol. 37, no. 1, pp. 150–161, Jan. 2022.
[53] I. Z. Petric, P. Mattavelli, and S. Buso, "Investigation of nonlinearities introduced by multi-sampled pulsewidth modulators," *IEEE Trans. Power Electron.*, vol. 37, no. 3, pp. 2538–2550, Mar. 2022.
[54] I. Z. Petric, P. Mattavelli, and S. Buso, "Multi-sampled grid-connected VSCs: A path toward inherent admittance passivity," *IEEE Trans. Power Electron.*, vol. 37, no. 7, pp. 7675–7687, Jul. 2022.
[55] H. d. T. Mouton, S. M. Cox, B. McGrath, L. Risbo, and B. Putzeys, "Small-signal analysis of naturally-sampled single-edge PWM control loops," *IEEE Trans. Power Electron.*, vol. 33, no. 1, pp. 51–64, Jan. 2018.
[56] R. Cvetanovic, I. Z. Petric, P. Mattavelli, and S. Buso, "Accurate high-frequency modeling of the input admittance of PWM grid-connected VSCs," *IEEE Trans. Power Electron.*, vol. 37, no. 9, pp. 10534–10545, Sep. 2022.
[57] D. Van de Sype, K. De Gusseme, A. Van den Bossche, and J. Melkebeek, "Small-signal laplace-domain analysis of uniformly-sampled pulse-width modulators," in *Proc. IEEE 35th Annu. Power Electron. Spec. Conf.*, 2004, vol. 6, pp. 4292–4298.
[58] R. Gupta, A. Ghosh, and A. Joshi, "Characteristic analysis for multi-sampled digital implementation of fixed-switching-frequency closed-loop modulation of voltage-source inverter," *IEEE Trans. Ind. Electron.*, vol. 56, no. 7, pp. 2382–2392, Jul. 2009.
[59] *Railway Applications—Power Supply and Rolling Stock—Technical Criteria for the Coordination Between Power Supply (Substation) and Rolling Stock to Achieve Interoperability*, *CENELEC Standard EN50388*, 2012.
[60] P. Mattavelli, F. Polo, F. Dal Lago, and S. Saggini, "Analysis of control-delay reduction for the improvement of ups voltage-loop bandwidth," *IEEE Trans. Ind. Electron.*, vol. 55, no. 8, pp. 2903–2911, Aug. 2008.
[61] D. Yang, X. Ruan, and H. Wu, "A real-time computation method with dual sampling mode to improve the current control performance of the *lcl*-type grid-connected inverter," *IEEE Trans. Ind. Electron.*, vol. 62, no. 7, pp. 4563–4572, Jul. 2015.
[62] S. K. Mitra and Y. Kuo, *Digital Signal Processing: A Computer-Based Approach*, vol. 2. New York, NY, USA: McGraw-Hill, 2006.
[63] W. Gardner, "Common pitfalls in the application of stationary process theory to time-sampled and modulated signals," *IEEE Trans. Commun.*, vol. COM-35, no. 5, pp. 529–534, May 1987.

Ivan Z. Petric (Student Member, IEEE) was born in Belgrade, Serbia, in 1994. He received the B.S. and M.S. degrees in electrical engineering from the University of Belgrade, Belgrade, Serbia, in 2017 and 2018, respectively. He is currently working toward the Ph.D. degree with Power Electronics Group, Department of Information Engineering, University of Padova, Padova, Italy.

From 2018 to 2019, he was a Researcher with the Power Electronics, Machines and Control Group, University of Nottingham, Nottingham, U.K. In 2022, he joined the Department of Electrical Engineering and Computer Sciences, University of California, Berkeley, CA, USA, as a Visiting Researcher. His research interests include modeling and digital control of power converters, grid-connected converters for renewable energy sources and smart microgrids, and electrical drives.

Paolo Mattavelli (Fellow, IEEE) received the M.S. (Hons.) and Ph.D. degrees in electrical engineering from the University of Padova, Padova, Italy, in 1992 and 1995, respectively.

From 1995 to 2001, he was a Researcher with the University of Padova. From 2001 to 2005, he was an Associate Professor with the University of Udine, Udine, Italy, where he led the Power Electronics Laboratory. In 2005, he joined the University of Padova, Vicenza, Italy, with the same duties. From 2010 to 2012, he was with the Center for Power Electronics Systems, Virginia Tech, Blacksburg, VA, USA. He is currently a Professor with the University of Padova, Vicenza. His current Google Scholar H-index is 82. He has been leading several industrial and government projects in his research fields. His research interests include analysis, modeling, and analog and digital control of power converters, grid-connected converters for renewable energy systems and microgrids, and high-temperature and high-power-density power electronics.

Dr. Mattavelli was an Associate Editor for IEEE TRANSACTIONS ON POWER ELECTRONICS, from 2003 to 2012. From 2005 to 2010, he was the Industrial Power Converter Committee Technical Review Chair for IEEE TRANSACTIONS ON INDUSTRY APPLICATIONS. For terms 2003–2006, 2006–2009, and 2013–2015, he was a Member-at-Large of the IEEE Power Electronics Society's Administrative Committee. He received the Prize Paper Award in IEEE TRANSACTIONS ON POWER ELECTRONICS in 2005, 2006, 2011, and 2012 and the second Prize Paper Award at the IEEE Industry Application Annual Meeting in 2007. He is the Co-Editor-in-Chief for IEEE TRANSACTIONS ON POWER ELECTRONICS.

Simone Buso (Member, IEEE) received the M.Sc. degree in electronic engineering and the Ph.D. degree in industrial electronics from the University of Padova, Padova, Italy, in 1992 and 1997, respectively.

He is currently an Associate Professor of Electronics with the Department of Information Engineering, University of Padova. His main research interests are in the industrial and power electronics fields and include switching converter topologies, digital control of power converters, renewable energy sources, and smart microgrids.